Available online at www.sciencedirect.com
SCIENCE DIRECT®
Journal of Catalysis 222 (2004) 87–99
JOURNAL OF CATALYSIS
www.elsevier.com/locate/jcat

Transient kinetic model of CO oxidation over a nanostructured $Cu_{0.1}Ce_{0.9}O_{2-y}$ catalyst

Gregor Sedmak,[a] Stanko Hočevar,[a,*] and Janez Levec [a,b]

[a] *Laboratory of Catalysis and Reaction Engineering, National Institute of Chemistry, Hajdrihova 19, PO Box 660, SI-1000 Ljubljana, Slovenia*
[b] *Department of Chemistry and Chemical Technology, University of Ljubljana, Aškerčeva 5, SI-1000 Ljubljana, Slovenia*

Received 2 July 2003; revised 12 September 2003; accepted 8 October 2003

Abstract

The oxidation of carbon monoxide under dynamic conditions was studied over a novel nanostructured $Cu_{0.1}Ce_{0.9}O_{2-y}$ catalyst. CO temperature-programmed reduction provides a qualitative picture of the reducibility of that catalyst. Step-change experiments in CO concentration in the temperature range between 50 and 250 °C allowed us to estimate the oxygen storage capacity of the catalyst as a function of temperature. The measured CO and CO_2 responses were used to construct a detailed transient kinetic model based on elementary reaction steps. In the modeling, elementary reaction steps such as the adsorption of CO on oxidized and reduced catalyst active sites, diffusion of subsurface lattice oxygen to the surface, reoxidation of reduced catalyst active sites by the subsurface lattice oxygen, and the surface reaction of CO to CO_2 were considered. The calculated activation energies for various surface reaction steps were in the range from 9.7 to 39.6 kJ mol^{-1}, for the catalyst reoxidation step 72.9 kJ mol^{-1}, and for the lattice oxygen diffusion in the $Cu_{0.1}Ce_{0.9}O_{2-y}$ catalyst 40.0 kJ mol^{-1}. These values are discussed in detail. The bulk oxygen diffusion coefficient is equal to 3.2×10^{-12} cm^2 s^{-1} at 250 °C. This value is in the range of bulk diffusion coefficients measured over other oxide catalysts.

Keywords: Transient kinetics; Kinetic model; $Cu_{0.1}Ce_{0.9}O_{2-y}$ catalyst; CO oxidation; Redox process; Lattice oxygen diffusion; PROX; Fuel cell

1. Introduction

Fuel cell power generation has experienced rapid development in recent years for both stationary and vehicle applications. In the transportation sector, hydrogen-fueled, proton-exchange membrane (PEM) fuel cells hold considerable potential for replacing conventional internal combustion engines. Fuel cell technology not only meets the most stringent emission regulations but also possesses the necessary specific power, power density, and durability. In order to avoid problems associated with hydrogen distribution and storage, H_2 can be produced on board by autothermal reforming of hydrogen-rich fuels, preferably renewable ones, such as methanol. Generally, the reformate gas typically contains H_2, CO_2, H_2O, traces of unconverted fuel, and, unfortunately, 0.5–2 vol% CO. It is imperative to lower the concentration of carbon monoxide in the reformer gas below 100 ppm not only because it is a criterion pollutant but also because it is a catalyst poison for the fuel cell Pt gas-diffusion anode. Of the currently available methods for removing CO from a hydrogen-rich atmosphere, the selective catalytic oxidation of CO is the most straightforward, simple, and cost-effective one.

The novel nanostructured $Cu_{0.1}Ce_{0.9}O_{2-y}$ catalyst is proven to be capable of oxidizing CO at high conversion in excess of hydrogen with 100% selectivity at 90 °C [1–5]. The selectivity at temperatures higher than 90 °C is a function of stoichiometric ratio of O_2 and CO [4]. Concentrations of oxygen higher than that required to oxidize CO to CO_2 result in oxidation of H_2 to water. Thus, to keep the selectivity of the CO oxidation reaction over nanostructured $Cu_{0.1}Ce_{0.9}O_{2-y}$ catalysts in excess of hydrogen as high as possible, the amount of oxygen supplied to a preferential oxidation (PROX) reactor must be as close to a stoichiometric ratio as possible. However, the high capacity of $Cu_{0.1}Ce_{0.9}O_{2-y}$-nanostructured catalysts to store oxygen [6] can be used to cope with rapid changes in the concentration of CO in the PROX reactor inlet stream if it operates under dynamic conditions. If the PROX reactor operates un-

* Corresponding author.
E-mail address: stanko.hocevar@ki.si (S. Hočevar).

0021-9517/$ – see front matter
doi:10.1016/j.jcat.2003.10.006

der oxygen rich conditions, it stores oxygen, while under oxygen-lean conditions, the catalyst releases oxygen. If, at some instant, the amount of gas-phase oxygen is not high enough to completely oxidize CO, it can be supplied by the catalyst itself. In this way, no breakthrough of CO in the PROX reactor outlet stream and the highest selectivity of CO oxidation reaction are assured.

If the PROX reactor is to be used on board, it is necessary to study the behavior of carbon monoxide oxidation under transient conditions. The basic principle in studying the dynamic behavior of catalytic reactors is as follows: the composition of an open reactor inlet stream is perturbed by a step, pulse, or a square-wave function and the response of a system is measured. A transient kinetic model can be constructed that adequately describes changes in CO and CO_2 concentrations in the PROX reactor effluent stream operated under dynamic conditions. However, a transient kinetic model is not only important for accurate simulation of the reactor but also provides a detailed insight in the underlying reaction mechanism [7]. It is also an important tool for designing commercial reactors. Analysis of data measured under steady-state conditions, usually, leads to global models that do not permit a description of the dynamic behavior of heterogeneous catalytic reactors for different values of the input parameters. For this purpose, it is necessary to have models of the individual steps, which, however, are very difficult to obtain from steady-state experiments [8].

A lot of studies on catalytic oxidation of carbon monoxide under dynamic conditions refer to the reaction proceeding over supported noble metal catalysts [7–14]. The number of studies regarding CO oxidation over oxide catalysts is substantially lower [15,16]. Even less is the number of studies that include elementary-step modeling of the diffusion of subsurface lattice oxygen in carbon monoxide oxidation over oxide catalysts. One of the very few is the study regarding oxidation of CO over silica-supported Fe_2O_3 [17].

In the present study we report on the dynamic oxidation of carbon monoxide over a nanostructured $Cu_{0.1}Ce_{0.9}O_{2-y}$ catalyst. First, CO temperature-programmed reduction of the catalyst was employed to get a qualitative picture of reducibility of that catalyst. Next, step-change experiments in CO concentration were used. With the help of those experiments, the oxygen-storage capacity of the catalyst was quantified in the temperature range between 50 and 250 °C. A detailed elementary-step model of the CO oxidation over a $Cu_{0.1}Ce_{0.9}O_{2-y}$-nanostructured catalyst under dynamic conditions was developed. The model discriminates between adsorption of carbon monoxide on catalyst inert sites, as well as on oxidized and reduced catalyst active sites. Apart from that, the diffusion of subsurface species in the catalyst and the reoxidation of reduced catalyst sites by subsurface lattice oxygen species were considered in the model. The model allows us to calculate activation energies of all elementary steps considered as well as the bulk diffusion coefficient of oxygen species in the nanostructured $Cu_{0.1}Ce_{0.9}O_{2-y}$ catalyst. The diffusion coefficient obtained by the mathematical modeling of step experiments is shown to be in the range of bulk diffusion coefficients measured over other oxide catalysts.

2. Experimental

2.1. Catalyst preparation and characterization

The $Cu_{0.1}Ce_{0.9}O_{2-y}$-nanostructured catalyst was synthesized by a sol-gel method as described in [18]. The catalyst was then calcined at 650 °C for 1 h in a flow of dry air. Catalyst powder was then used in the experiments. The particle size of a catalyst was measured by a particle-size analyzer (Microtrac, FRA9200). Catalyst-specific surface area was the same as reported in [4].

2.2. The experimental setup

The experimental setup consisted of a feed, reactor, and gas analysis sections. The feed section consisted of two separate feed lines converging at a four-way chromatographic valve (Valco), by which almost instant switching between feed sections could be achieved. This eliminated overshoot of the concentration step change (forcing function) that would result from the stopping of the flow through the valve [19].

Reactant gases (Messer Slovenia) were metered by calibrated mass flow controllers. In all experiments, He was used as a diluent gas. In order to assure a stable flow of carbon monoxide, mixtures of CO in He with appropriate concentrations were prepared in a separate cylinder. In temperature-programmed reduction (TPR) studies, 1 vol% CO in helium was used. In transient concentration step experiments, mixtures of 0.5, 1, and 2 vol% CO in Helium were prepared.

The reactor consisted of a 4.6-mm-i.d. × 230-mm-long glass tube inserted into a heated aluminum block. The reactor temperature was measured by a K-type thermocouple located in the middle of the aluminum block close to the reactor tube and regulated by a PID temperature controller (Shimaden SR25). In TPR studies, temperature was varied between 30 and 400 °C, while in CO transient step experiments, it was varied between 50 and 250 °C.

In some preliminary studies, the catalyst powder obtained after calcination was pelleted and sieved into fractions of various sizes between 0.1 and 0.6 mm. It was found that at temperatures above 225 °C, the catalyst effectiveness factor [20] drops below 1, thus signifying the presence of concentration gradients inside catalyst pellets. For this reason, the catalyst was not pelleted at all in further experiments. The mean particle size of such a catalyst powder was equal to 15 μm, while the particle-size distribution was in the range from 3 to 50 μm. It was found also that volumetric flow rate of 200 mL/min under standard conditions eliminates external mass-transport resistance at a reaction temperature of 250 °C.

The temperature in the catalyst bed was measured in a preliminary experiment. It was done by inserting another thermocouple axially into reactor tube. It was found that in CO step-change experiments, the catalyst bed temperature was raised 10 °C. For that reason, the catalyst was diluted with quartz beads with a dilution ratio 1:8 by mass. This reduced the increases of the catalyst bed temperature below 0.9 °C, which assures the isothermal conditions. The fraction of quartz beads used in the experiments ranged from 160 to 315 μm to avoid a large pressure drop along the reactor.

Mass of catalyst used in experiments was always 200 mg. Catalyst and quartz beads were loaded into the reactor in such a way that no catalyst segregation occurred. The diluted catalyst bed was embedded with pure quartz beads on both sides. This arrangement was secured by glass wool on both sides to keep the bed in a fixed position.

Responses to the step changes in the concentration of feed components were measured by a quadrupole mass spectrometer (QM) (Leybold PGA 100). A signal was recorded and analyzed by a PC via RS232 connection. Great care was devoted to use as short conduits as possible between the four-way chromatographic valve and reactor entrance and also between the reactor exit and capillary that connects reactor and QM module. Preliminary studies with 1 vol% argon in helium showed that the reactor could be regarded as an ideal plug-flow reactor. The concentration step change in the reactor inlet stream obtained by switching the four-way valve could be regarded as an ideal step change (see Section 3.2).

During CO-TPR experiments, intensities in QM signal were small and did not allow absolute quantification of reaction components. However, because the signal/noise ratio was still at least 20/1, semiquantification could be achieved. Because of that, the CO and CO_2 signals are not reported in partial pressure units but in arbitrary units. In transient step experiments, QM signals were much more pronounced. In that case, absolute quantification of CO and CO_2 could be achieved. The QM was calibrated with gas mixtures of known composition. Concentrations of CO or CO_2 in reactor effluent stream were then obtained by subtraction of the baseline from the signal. The signal corresponding to carbon monoxide at $m/e = 28$ was corrected further for the error that is caused by overlapping with CO signal that is caused by CO_2 fragmentation.

2.3. The procedure

Prior to all experiments the catalyst was pretreated in situ with a mixture of 20 vol% O_2 in He (100 mL/min) at 400 °C for 30 min. In order to obtain reproducible kinetic data, the pretreatment procedure was followed by the in situ steady-state lineout procedure. The lineout procedure is described in detail in [4].

The CO temperature-programmed reduction of the catalyst was performed using the following procedure: before every run, the catalyst pretreatment was employed to reoxidize completely the catalyst and to clean its surface. Then the catalyst temperature was lowered to 30 °C under the same atmosphere of flowing gases. Next, the flow of oxygen was stopped and the catalyst was purged with He (100 mL/min) for 1 h. The flow of He was then replaced with 1 vol% CO/He (100 mL/min) and after 1 min, the temperature ramp of 10 °C/min was started until a temperature of 400 °C was reached.

Before every CO transient kinetic experiment, the same catalyst pretreatment procedure as in the CO TPR experiments was used. When the pretreatment procedure was over, the catalyst was cooled to 250 °C under the same flow of gases. Then, the flow of oxygen was stopped and the flow of He was increased to 200 mL/min. After 1 h of He purge at 250 °C the reactor temperature was set to the desired value. Next, the QM spectrometer was calibrated and a transient experiment was performed.

When transient kinetic experiments were performed, one batch of catalyst was used in 15 transient runs. After that, a new batch of catalyst was used. The activity and stability of a batch of catalyst when treated in such a manner remain virtually unchanged [4].

3. Reaction mechanism

3.1. CO-TPR of the $Cu_{0.1}Ce_{0.9}O_{2-y}$-nanostructured catalyst

Fig. 1 shows the CO reduction profile of the nanostructured $Cu_{0.1}Ce_{0.9}O_{2-y}$ catalyst. In the figure the CO-consumption line is designated by a dashed curve, while the CO_2-formation line by a solid curve. Both lines are strictly concomitant. Two reduction peaks can be observed: the low-temperature reduction peak with a maximum at 70 °C and a high-temperature reduction peak that starts rising at 125 °C and has a maximum at 250 °C.

The CO-TPR profile of the nanostructured $Cu_{0.1}Ce_{0.9}O_{2-y}$ catalyst prepared by the sol–gel method is similar in

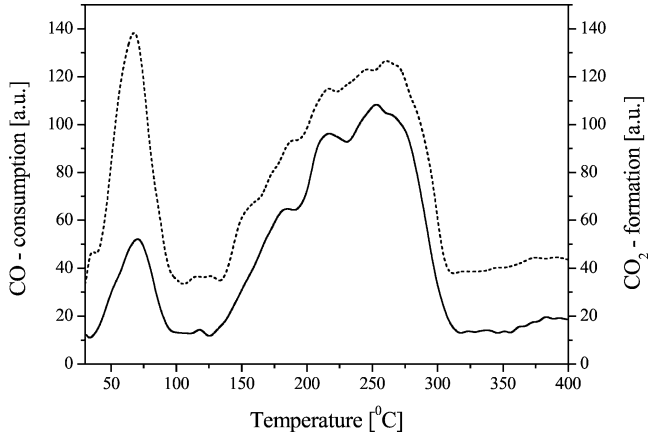

Fig. 1. CO TPR profile of nanostructured $Cu_{0.1}Ce_{0.9}O_{2-y}$ catalyst with a CO-consumption line (- - -) and CO_2-formation line (—). Conditions: $m_{cat} = 200$ mg, $\Phi_v = 100$ mL min^{-1}.

nature to the H_2-TPR profile of that catalyst prepared by a coprecipitation [21,22] and impregnation [23] method. The difference between the H_2- and CO-TPR profiles is in the position of the first and second reduction peak. The catalyst reduction peaks in CO appear at lower temperatures than those in H_2. This could be explained by the fact that CO has higher reducing capabilities than H_2 of the nanostructured $Cu_{0.1}Ce_{0.9}O_{2-y}$ catalyst [4,24,25]. Besides that, preparation route of the $Cu_{0.1}Ce_{0.9}O_{2-y}$-nanostructured catalyst employed in the present study differs from the preparation route described in [21–23]. However, it is generally agreed that the first peak is due to the reduction of the CuO component that is finely dispersed on the catalyst surface. Bulk CeO_2 and CuO reduction is the reason for the second structured and broad reduction peak.

The only difference between the CO-consumption and CO_2-formation lines from Fig. 1 is in the area of the first, low-temperature peak (Fig. 1). The area of low-temperature CO_2-formation peak is around two times smaller than the area of a CO-consumption peak. The reason for this is the fact that when the CO-TPR is started, some amount of CO is left adsorbed on the catalyst surface and it does not convert to CO_2. It is a consequence of a complex microstructure of the $Cu_{0.1}Ce_{0.9}O_{2-y}$-nanostructured catalyst where several different copper and cerium oxide domains exist in different proportions [4,21,22]. The sites that are not active for CO oxidation are named as catalyst inert sites in this paper.

3.2. CO concentration step-change experiments

Fig. 2 represents the CO and CO_2 responses after a step change from He to 1 vol% CO/He over the fully oxidized $Cu_{0.1}Ce_{0.9}O_{2-y}$-nanostructured catalyst. At low temperatures, CO breakthrough is delayed for a few seconds as can be seen from Fig. 2a. At a temperature of 250 °C, however, 20 s is needed for the first traces of CO to exit the reactor. On the other hand, the evolution of CO_2 in the reactor effluent stream has no delay as represented on Fig. 2b. However, the nature of the CO_2 peak as a function of temperature changes significantly. At temperatures lower than 100 °C only one peak in CO_2 response is visible. At 100 °C the CO_2 peak broadens and at 125 °C two separate peaks are clearly visible. The first peak is narrow, followed by a second broader peak. When the temperature is raised further, the first peak in the CO_2 response becomes invisible, because it is overridden by the second peak. Only the origin of first peak is signified by a fast evolution of CO_2 in the reactor effluent stream. It is also important to note how the maximum of the second peak shifts to the right when the temperature is raised. At 250 °C the catalyst surface responds almost instantly to a CO step change by producing CO_2. The concentration of CO_2 in the reactor effluent gas after 3 s is 0.65 vol% as shown in Fig. 2b. However, the CO_2 concentration in the reactor effluent gas rises further and reaches 0.80 vol% after 25 s. This is followed by a sharp decrease in the CO_2 concentration which stabilizes after 100 s at 0.2 vol%. Afterward the concentration in CO_2 decreases very slowly and falls to zero after 13 min.

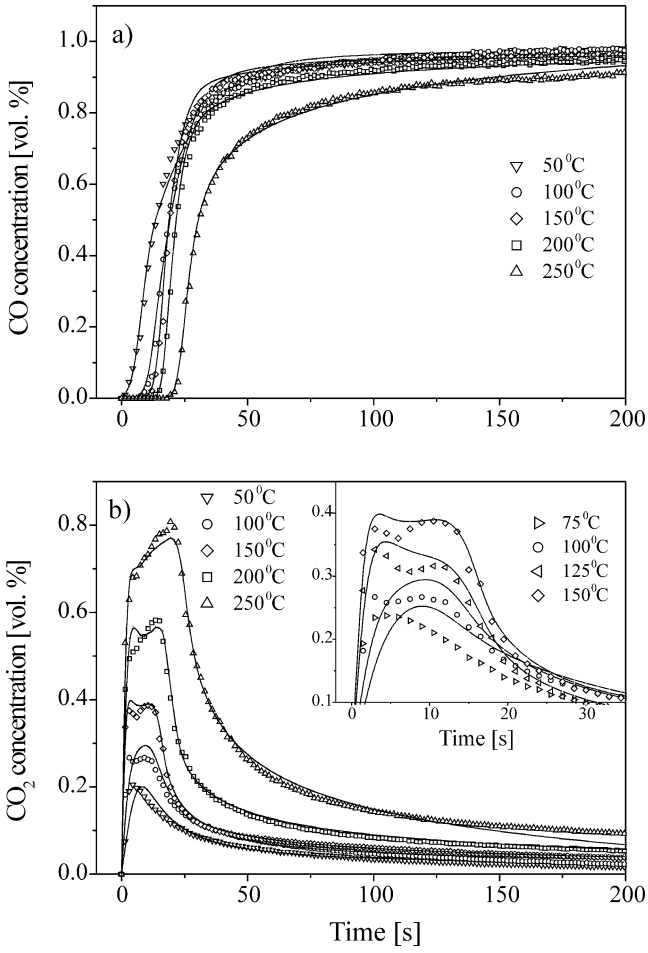

Fig. 2. (a) CO and (b) CO_2 concentrations in the reactor effluent stream as a function of temperature. The markers represent experimental points. The solid lines represent the model predictions obtained by the integration of the rate equations given in Table 3 with initial and boundary conditions given in Table 4. The kinetic parameter values are given in Table 5. The catalyst capacities are equal to $L_{TOT} = 0.030\ \text{mol kg}_{cat}^{-1}$ and $H_{TOT} = 0.35\ \text{mol kg}_{cat}^{-1}$. F_{TOT} values correspond to Table 1 subtracted by $0.030\ \text{mol kg}_{cat}^{-1}$. Conditions: $m_{cat} = 200$ mg, $\Phi_v = 200\ \text{mL min}^{-1}$. For the sake of clearness not all of the measured and response curves are presented.

Fig. 3 shows the carbon mass balance in the reactor effluent stream, which is represented by the sum of CO and CO_2 concentrations. This is not ideal, since there is always some lack of carbon species at the beginning of a concentration step. At longer times, carbon mass balance approaches ideal values. As a reference, the QM response to a concentration step from He to 1 vol% Ar/He is shown. This concentration step can be regarded as ideal. The initial deviation in carbon mass balance from ideal behavior signifies that some amount of CO stays adsorbed on the catalyst inert sites. This is the same phenomenon as was already observed in CO-TPR experiments (Fig. 1). By integrating the carbon mass balance curves obtained by concentration step experiments, the exact amount of CO adsorbed on the catalyst inert sites could be

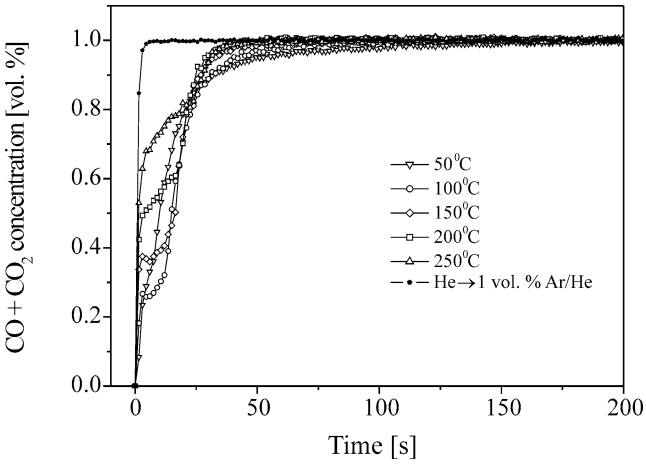

Fig. 3. Carbon mass balance represented as a sum of CO and CO_2 concentrations in the reactor effluent stream. As a reference, a concentration step from He to 1 vol% Ar/He is provided.

Table 1
Variation of the adsorptive surface capacity of carbon monoxide over a nanostructured $Cu_{0.1}Ce_{0.9}O_{2-y}$ catalyst as a function of reaction temperature

Reaction temperature (°C)	Overall CO adsorptive capacity (mol kg_{cat}^{-1})
50	0.100
75	0.100
100	0.095
125	0.090
150	0.080
175	0.075
200	0.065
225	0.060
250	0.050

calculated (Table 1). As can be expected, the adsorptive capacity decreases when the reaction temperature is increased.

3.3. Mechanism of transient CO oxidation over a completely oxidized catalyst

Fig. 4 shows the oxygen-storage capacity (OSC) of the $Cu_{0.1}Ce_{0.9}O_{2-y}$-nanostructured catalyst at temperatures between 50 and 250 °C obtained by concentration step experiments with 1 vol% CO/He. The oxygen-storage capacity of the same catalyst measured at 400 °C was found to be 1.23 mol CO_2 kg_{cat}^{-1} [4]. If we convert the amount of consumed oxygen to the area that it occupies in the physisorbed state, a little less than one monolayer of oxygen would be consumed in the CO oxidation reaction at 250 °C [26]. At 400 °C, it would amount to 2.3 monolayers [4]. However, as it will be explained in Section 4, only a very small amount of oxygen needed to oxidize CO has the origin in the physisorbed layer.

The oxygen-storage capacity of the catalyst was found to be dependent on concentration of CO in helium. The reason for this is the different reduction potential of the gas phase.

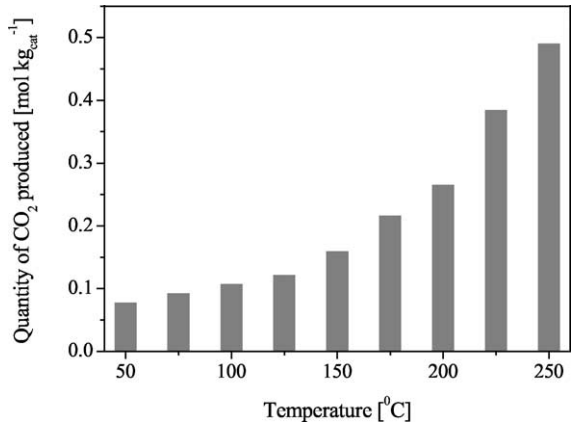

Fig. 4. Oxygen-storage capacity of the $Cu_{0.1}Ce_{0.9}O_{2-y}$-nanostructured catalyst as a function of reaction temperature obtained by concentration step experiments with 1 vol% CO/He. The OSC was obtained by integration of the area under the CO_2 response curves.

When concentration steps with 0.5 vol% CO/He were used, the values of OSC were 30% lower than those reported in Fig. 4. When the concentration steps with 2 vol% CO/He were used, no difference was observed.

From the CO and CO_2 responses over the fully oxidized catalyst some conclusions can be drawn. The initial delay of CO in the reactor effluent stream signifies that CO adsorbs instantly on the catalyst surface. It then reacts very quickly to CO_2. Carbon monoxide was therefore adsorbed on a site already covered by oxygen. If CO and O_2 were competing for the adsorption sites on the catalyst, the preadsorbed oxygen would inhibit adsorption of carbon monoxide. As a consequence, the classical Langmuir–Hinshelwood reaction scheme involving competitive adsorption of CO and O_2 followed by a bimolecular surface reaction is ruled out as a possible reaction mechanism. Moreover, CO oxidation without the presence of oxygen in the reactor feed does not proceed by any type of simple or more complex combination of surface reactions of the Langmuir–Hinshelwood type [27].

It was shown that the creation of oxygen vacancies on the CeO_2 surface significantly promotes the oxidation of carbon monoxide [28]. Another simulation of oxidation of carbon monoxide over pure CuO showed that the reduction process of CuO proceeds in two steps. In the first step surface oxygen is removed while in the second step, bulk oxygen starts to react [29]. It was shown that CO reduces the surface of CeO_2 [30] and CuO/CeO_2 [31] catalysts even at room temperature.

It is generally accepted that CuO and CeO_2 have a great synergistic effect when those two substances are prepared as a composite CuO/CeO_2 catalyst. The reason for that is probably the formation of a solid solution of CuO and CeO_2 phases [32]. The amount of solid solution between those two phases, however, is small [18,23,33–35]. Most probably, the substitutional solid solution forms tiny intergrowths at the interface between XRD amorphous CuO and nanocrystalline CeO_2 phases [4,36]. The substitutional solid solution is most probably sandwiched between the dispersed CuO clusters

Table 2
Elementary reaction steps considered in the kinetic modeling of the CO concentration step-change experiments for the oxidation of CO over a completely oxidized $Cu_{0.1}Ce_{0.9}O_{2-y}$-nanostructured catalyst without the presence of oxygen in the reactor feed

Step No.	Elementary reaction step
1	$CO + Cu^{2+}O_{s,s} \xrightarrow{k_1} CO\cdots Cu^{2+}O_{s,s}$
2	$CO\cdots Cu^{2+}O_{s,s} \xrightarrow{k_2} CO_2 + Cu^{+}\square_s$
3	$CO + Cu^{+}\square_s \xrightarrow{k_3} CO\cdots Cu^{+}\square_s$
4	$Ce^{4+}O_{b,b} \xrightarrow{D} Ce^{3+}\square_b + O_{s,b}$
5	$CO\cdots Cu^{+}\square_s + O_{s,b} \xrightarrow{k_4} CO\cdots Cu^{2+}O_{s,b}$
6	$CO\cdots Cu^{2+}O_{s,b} \xrightarrow{k_2} CO_2 + Cu^{+}\square_s$
7	$CO + * \xrightarrow{k_5} CO*$
	$2CO + Cu^{2+}O_{s,s} + Ce^{4+}O_{b,b} \rightarrow 2CO_2 + Cu^{+}\square_s + Ce^{3+}\square_b$

Oxygen vacancy is represented by □. The meaning of subscripts accompanying oxygen species and oxygen vacancies is explained in the text.

and the CeO_2 crystallites [18], which is called the interfacial region in this article. This interface might have a thickness of only a few atomic layers. When the Cu^{2+} species reduces to Cu^{1+} state, it is subsequently reoxidized by reduction of the Ce^{4+} ions in their vicinity into Ce^{3+} and the following redox equilibrium is established [4,36–38]:

$$Ce^{4+} + Cu^{1+} \rightleftarrows Ce^{3+} + Cu^{2+}. \quad (1)$$

This equilibrium has a buffer-like effect, stabilizing the presence of cationic copper species in the structure even in a highly reductive atmosphere. The above scheme of copper oxide–ceria interactions indicates clearly that CuO/CeO_2 catalyst is bifunctionally promoted. That means both copper and ceria cooperate in the redox mechanism.

When oxygen vacancy is created upon lattice oxygen extraction, the CuO/CeO_2 catalyst becomes an electrical conductor [39]. In another study it was shown that the activation energy for oxygen ion diffusivity in a $Ce_{0.69}Gd_{0.31}O_{2-y}$ catalyst measured by isotope tracer studies on a single crystal has a similar value as the one obtained from measurements of electrical conductivity when converted to an oxygen self-diffusion coefficient using the Nernst–Einstein equation [40]. This suggests that the two processes of lattice oxygen self-diffusion and electron conduction are in fact very similar in nature, so the charge transfer does not produce any inhibiting effects on the kinetics of the redox reaction.

The individual elementary steps considered in the kinetic modeling of the CO concentration step-change experiments for the oxidation of CO over completely oxidized nanostructured $Cu_{0.1}Ce_{0.9}O_{2-y}$ catalysts without the presence of oxygen in the reactor feed are shown in Table 2. The subscripts accompanying oxygen species have the following meaning: the first subscript designates the present location of oxygen species, while the second subscript designates the history of oxygen species. The designation like $O_{s,b}$ should be read as: "oxygen species that is presently located on the catalyst surface but it diffused from the bulk of catalyst crystal lattice." When the oxygen species reacts with CO into CO_2, no difference in history is tracked any more. The subscripts accompanying oxygen vacancies represent the location of the vacancy.

The reaction mechanism is composed of seven different elementary steps which proceed both consecutively and in parallel. In the first step, CO adsorbs on the copper/ceria interfacial region of the catalyst, the most reactive phase for the CO oxidation reaction [4]. Most probably, copper cations serve as adsorption sites for carbon monoxide [31, 41–43]. Before the reaction of oxidation of carbon monoxide is started, copper is found in a fully oxidized state [31,41] as represented by $Cu^{2+}O_{s,s}$. After the CO molecule adsorbs on the catalyst active sites (copper cation), it extracts oxygen from the surface and leaves an oxygen vacancy behind. Simultaneously, Cu^{2+} reduces to Cu^{+} as represented in step 2. This process is the reason for the very fast response of a preoxidized catalyst surface to the He → CO/He step as shown in Fig. 2b. In step 3, an additional quantity of carbon monoxide from the gas phase adsorbs on a partially reduced copper Cu^{+} species as represented by $CO\cdots Cu^{+}\square_s$. Cu^{+} sites are believed to be even better CO adsorption sites if compared to Cu^{2+} sites [43]. Because of the reduction of copper species from Cu^{2+} to Cu^{+} the number of surface oxygen vacancies increases. As a result, the potential difference between the concentration of oxygen on the surface of the catalyst and in the catalyst bulk is also increasing. Due to this concentration gradient, subsurface lattice oxygen starts to diffuse to the catalyst surface. When bulk oxygen reaches the surface, it swaps the position between cerium and copper cations located at the interfacial position. The net consequence of this transposition is the formation of a bulk oxygen vacancy in cerium oxide and, simultaneously, the reoxidation of surface copper oxide by subsurface lattice oxygen. This is represented by reaction steps 4 and 5. Cerium oxide acts as an oxygen supplier when it is needed at the place of the reaction. Reaction step 6 is in fact analogous to reaction step 2. In both steps, a preadsorbed CO molecule extracts oxygen from oxidized copper(II) oxide. The only difference between those two steps is the origin of oxygen species that participate in the reaction. In step 2, oxygen that is originally present on the catalyst surface is involved in the reaction. In step 6, surface oxygen that diffused from the subsurface regions is involved in the reaction. In both steps the same copper cation is involved. Because the only difference between the $Cu^{2+}O_{s,s}$ and the $Cu^{2+}O_{s,b}$ species is the history of oxygen atom, but not the present state, the adsorbed CO molecule does not feel the difference between those two species. This is why both reaction step 2 and reaction step 6 share the same kinetic rate constant (k_2). Those two reactions proceed in parallel as long as there is some oxygen species $O_{s,s}$ left on the surface. When all $O_{s,s}$ species is consumed, only bulk oxygen participates in the CO oxidation reaction. Reaction step 6 is responsible for the second, broader peak in CO_2 signal (Fig. 2b) as already de-

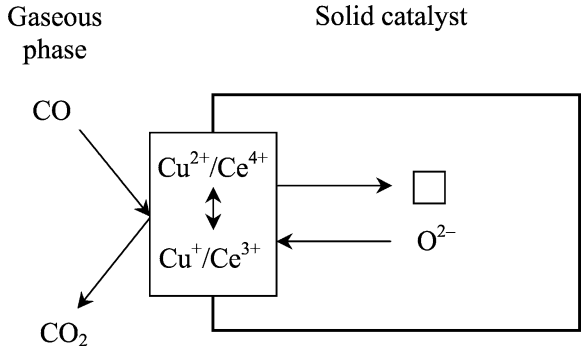

Fig. 5. Scheme of the redox mechanism for CO oxidation over an initially completely oxidized nanostructured $Cu_{0.1}Ce_{0.9}O_{2-y}$ catalyst. The enhanced reactivity at the interface of CuO and CeO_2 phases is presented. Since there is no oxygen in the reactor feed, the reoxidation of catalyst active sites can proceed only by the diffusion of oxygen through the bulk of catalyst crystal lattice.

scribed in Section 3.2. After longer reduction of the catalyst by a CO/He flow, the catalyst surface is populated only by two species: $CO\cdots Cu^{+}\square_s$ species representing a CO molecule adsorbed on a reduced catalyst active site as well as a $CO\cdots Cu^{2+}O_{s,b}$ species representing adsorbed CO molecule on catalyst active site which is freshly reoxidized by the subsurface lattice oxygen. The reaction of oxidation of carbon monoxide proceeds as long as there is enough subsurface lattice oxygen available. When also bulk oxygen is consumed, the CO oxidation reaction stops. Reaction step 7 represents adsorption of a CO molecule on the catalyst inert site (∗). The overall reaction mechanism is schematically presented in Fig. 5.

3.4. Model equations and parameters estimation

Table 3 shows the mass balance equations that correspond to the elementary reaction steps that are given in Table 2. Those equations involve mass balances of gas-phase CO and CO_2, catalyst surface species $Cu^{2+}O_{s,s}$, $CO\cdots Cu^{2+}O_{s,s}$, $Cu^{+}\square_s$, $CO\cdots Cu^{+}\square_s$, $CO\cdots Cu^{2+}O_{s,b}$, and CO*, as well as the diffusion of lattice oxygen. Variables and parameters that are used in those equations are defined in Section 6. The space time τ is defined as $\tau = \varepsilon_B m_{cat}/(\Phi_V \rho_B)$.

A recent TEM analysis of the nanostructured $Cu_{0.1}Ce_{0.9}O_{2-y}$ catalyst showed that it is composed of a number of tiny needles and platelets [44]. The elemental analysis of needles reveals that they are composed of copper, cerium, and oxygen, while the platelets contain only copper and oxygen. Because of that it is believed that active sites for CO oxidation lie on those needles. The diffusion equation of oxygen was therefore written in cylindrical coordinates. The characteristic diffusion time, t_d, is defined as R^2/D. H_{TOT} and $\xi_{Ob,b}$ are defined as volumetric capacity of catalyst phase and fractional volumetric "coverage" of oxygen species. In other words, the total number of oxygen species that can be extracted from the volume of completely oxidized crystallite needle is defined by H_{TOT}, while $(1-\xi_{Ob,b})$ defines the number of oxygen species that is extracted from the volume of crystallite needle divided by H_{TOT}.

Table 3
Mass balance equations for gas phase, surface and subsurface species corresponding to elementary reaction steps given in Table 2

$$\frac{\partial y_{CO}}{\partial t} + \frac{1}{\tau}\frac{\partial y_{CO}}{\partial z} = \frac{\rho_B}{\varepsilon_B}\left(-k_1 L_{TOT} y_{CO}\theta_{Cu^{2+}O_{s,s}} - k_3 L_{TOT} y_{CO}\theta_{Cu^{+}\square_s} - k_5 F_{TOT} y_{CO}\delta_*\right)$$

$$\frac{\partial y_{CO_2}}{\partial t} + \frac{1}{\tau}\frac{\partial y_{CO_2}}{\partial z} = \frac{\rho_B}{\varepsilon_B} k_2 (L_{TOT}/C_{TOT})\left(\theta_{CO\cdots Cu^{2+}O_{s,s}} + \theta_{CO\cdots Cu^{2+}O_{s,b}}\right)$$

$$\frac{\partial \theta_{Cu^{2+}O_{s,s}}}{\partial t} = -k_1 C_{TOT} y_{CO}\theta_{Cu^{2+}O_{s,s}}$$

$$\frac{\partial \theta_{CO\cdots Cu^{2+}O_{s,s}}}{\partial t} = k_1 C_{TOT} y_{CO}\theta_{Cu^{2+}O_{s,s}} - k_2\theta_{CO\cdots Cu^{2+}O_{s,s}}$$

$$\frac{\partial \theta_{Cu^{+}\square_s}}{\partial t} = k_2(\theta_{CO\cdots Cu^{2+}O_{s,s}} + \theta_{CO\cdots Cu^{2+}O_{s,b}}) - k_3 C_{TOT} y_{CO}\theta_{Cu^{+}\square_s}$$

$$\frac{\partial \theta_{CO\cdots Cu^{+}\square_s}}{\partial t} = k_3 C_{TOT} y_{CO}\theta_{Cu^{+}\square_s} - k_4 H_{TOT}\theta_{CO\cdots Cu^{+}\square_s}\xi_{O_{s,b}}$$

$$\frac{\partial \theta_{CO\cdots Cu^{2+}O_{s,b}}}{\partial t} = k_4 H_{TOT}\theta_{CO\cdots Cu^{+}\square_s}\xi_{O_{s,b}} - k_2\theta_{CO\cdots Cu^{2+}O_{s,b}}$$

$$\frac{\partial \delta_*}{\partial t} = -k_5 C_{TOT} y_{CO}\delta_*$$

$$\frac{\partial \xi_{O_{b,b}}}{\partial t} = \frac{1}{t_d}\left(\frac{\partial^2 \xi_{O_{b,b}}}{\partial x^2} + \frac{1}{x}\frac{\partial \xi_{O_{b,b}}}{\partial x}\right)$$

Table 4
Initial and boundary conditions corresponding to mass balance equations given in Table 3

$$y_{CO}(z,0) = 0, \quad y_{CO}(0,t) = 0.01$$

$$y_{CO_2}(z,0) = 0, \quad y_{CO_2}(0,t) = 0$$

$$\theta_{Cu^{2+}O_{s,s}}(z,0) = 1$$

$$\theta_{CO\cdots Cu^{2+}O_{s,s}}(z,0) = 0$$

$$\theta_{Cu^{+}\square_s}(z,0) = 0$$

$$\theta_{CO\cdots Cu^{+}\square_s}(z,0) = 0$$

$$\theta_{CO\cdots Cu^{2+}O_{s,b}}(z,0) = 0$$

$$\delta_*(z,0) = 1$$

$$\xi_{O_{b,b}}(z,x,0) = 1$$

$$\frac{\partial \xi_{O_{b,b}}}{\partial x}(z,0,t) = 0$$

$$a\frac{1}{t_d}\frac{\partial \xi_{O_{b,b}}}{\partial x}(z,1,t) = -k_3 L_{TOT}\theta_{CO\cdots Cu^{+}\square_s}\xi_{O_{b,b}}(z,1,t)$$

Table 4 shows the initial and boundary conditions that apply to the mass balance equations given in Table 3. The catalyst is assumed to be completely oxidized before the concentration step from He to 1 vol% CO/He is applied. The second boundary condition that applies to diffusion equation states that only the amount of oxygen that is transported from the bulk of the catalyst to the catalyst surface can subsequently be used in the reaction on the catalyst surface [45]. This condition connects elementary reaction steps 4 and 5

(Table 2). In this boundary condition, the oxygen species $O_{b,b}$ at position $x = 1$ could equally be written as $O_{s,b}$.

The reaction rate coefficients (k_i) and the reverse characteristic diffusion time ($1/t_d$) are all assumed to be temperature activated. Those coefficients are described by equations of the Arrhenius form as follows:

$$k_i = A_i \cdot \exp(-E_i/RT),$$
$$1/t_d = A_{t_d} \cdot \exp(-E_{t_d}/RT). \quad (2)$$

The system of partial differential equations with the corresponding initial and boundary conditions was solved using the method of lines. This is a quasi finite-difference method. It discretizes space derivatives by finite differences. Thus, it reduces a partial differential equation into the system of ordinary differential equations [46]. The first-order space derivatives in z-direction were discretized by the backward-difference formula. The first- and second-order space derivatives in x-direction were discretized by the central-difference formula. Since the dynamics of CO-oxidation reaction to step changes in concentration of CO is slow in comparison with the residence time of gases in the reactor, concentration gradients along the z-axes are not very high. Besides that, the diffusion in the solid state is also quite a slow process, so there are also no high concentration gradients in the x-direction. As a result, 9 nodes in the z-direction and 16 nodes in the x-direction were enough for the solution of a system of differential equations to become independent of the number of nodes. Those equations were than integrated in time by a general-purpose differential equation solver with variable step size (Berkeley Madonna 7.0 [47]).

Estimation of kinetic parameters was performed by fitting of the calculated molar fractions of CO and CO_2 at the reactor outlet to their experimentally measured values. A downhill simplex optimization algorithm minimized the root-mean-square value between model predictions and experimental data [47] (the objective function).

The kinetic parameters of the CO concentration step-change reaction over completely oxidized nanostructured $Cu_{0.1}Ce_{0.9}O_{2-y}$ catalysts were estimated at nine different temperatures (from 50 to 250 °C with a 25 °C temperature interval) and a concentration of 1 vol% CO in He. Kinetic parameters as obtained from model calculations with 1 vol% CO in He could then adequately predict experimental responses with 0.5 and 2 vol% CO in He carried out at different temperatures.

4. Results of modeling and discussion

In the modeling equations of CO concentration step-change experiments given in Table 3, nine parameters exist: three capacities of three different catalyst phases and six kinetic terms (five kinetic constants and a characteristic diffusion time). In the first step of parameter optimization, the model was run with all nine parameters left open, so all three catalyst capacities were estimated.

From the parameter optimization procedure, the values of capacity of catalyst active phase, L_{TOT}, varied in the range from 0.020 to 0.040 mol kg_{cat}^{-1} in the entire temperature interval. The increase was not linear, but still, the trend was to obtain lower values at lower temperatures. The values of volumetric oxygen capacity, H_{TOT}, varied between 0.25 and 0.45 mol kg_{cat}^{-1}. Finally, it was found that the values of surface capacity of the catalyst inert phase, F_{TOT}, follow the same trend as the values of the overall CO-adsorptive capacity given in Table 1. The differences between the values of F_{TOT} and the values given in Table 1 are constant and equal to 0.030 mol kg_{cat}^{-1}. This value is equal to the middle value of L_{TOT}.

The values of all three catalyst phases, obtained by mathematical modeling, were estimated in the view of their physical soundness. This was done by comparing these capacity values to the values that can be calculated from the data of $Cu_{0.1}Ce_{0.9}O_{2-y}$ catalyst properties.

At first, the capacity of a catalyst active phase was estimated. One can calculate that 0.2 g of nanostructured $Cu_{0.1}Ce_{0.9}O_{2-y}$ catalyst contains 1.2×10^{-4} mol of Cu^{2+} cations. When we take into account the stoichiometry of CO oxidation reaction and divide this by catalyst mass, then the maximum capacity of the catalyst active phase would be 0.3 mol kg_{cat}^{-1} if all $Cu^{2+}O$ species were reduced into $Cu_2{}^{+}O$ ones. If we compare this value to the middle value of L_{TOT}, 0.030 mol kg_{cat}^{-1}, obtained by the optimization procedure, we see that 10% of all copper cations in the catalyst are accessible for CO adsorption, while the other 90% either lie in the subsurface regions of a catalyst or are otherwise inaccessible as active sites for CO adsorption. We can see that the mathematical modeling gives physically plausible results.

Total volumetric oxygen capacity of the catalyst was calculated from data on catalyst crystal structure. The lattice of $Cu_{0.1}Ce_{0.9}O_{2-y}$ catalyst was approximated by crystal structure of pure ceria. It has a face-centered cubic fluorite structure with a lattice constant equal to 5.41×10^{-10} m. Since one unit cell contains 8 oxygen atoms, it can be calculated that the total capacity of oxygen atoms is 11.6 mol kg_{cat}^{-1}. If we compare this value to the middle value of H_{TOT}, 0.35 mol kg_{cat}^{-1}, obtained from mathematical modeling, we see that 3.0% of all bulk lattice oxygen atoms of $Cu_{0.1}Ce_{0.9}O_{2-y}$ catalysts can be extracted by carbon monoxide. The mathematical modeling gives us again a physically credible assumption. Besides, the value of H_{TOT} agrees favorably with experimentally determined values for catalyst oxygen-storage capacity given in Fig. 4.

It is reported that the irreversible gas uptakes for CO adsorption over various copper-containing oxides have values between 0.004 and 0.060 mol kg_{cat}^{-1} measured at 200 °C [48]. The estimates of the catalyst surface capacities (L_{TOT} and F_{TOT}) obtained by the mathematical modeling are in agreement with those results.

In order to increase the robustness of the model, the number of open fitting parameters must be reduced to a minimum. Because of that, all subsequent calculations were per-

formed with fixed values of catalyst capacities. The capacity of catalyst active phase, L_{TOT}, and volumetric oxygen capacity, H_{TOT}, were taken to be temperature insensitive and fixed to values of 0.030 and 0.35 mol kg_{cat}^{-1}, respectively. The value of capacity of catalyst inert phase, F_{TOT}, was taken to be a function of temperature. The values for F_{TOT} were taken from Table 1 and reduced by 0.030 mol kg_{cat}^{-1}. In all subsequent calculations, only reaction kinetic constants and characteristic diffusion time were left as open parameters in the fitting procedure. This reduces the number of open fitting parameters from 9 to 6.

The kinetic model that is described by equations given in Table 3 predicts very accurately the concentrations of CO and CO_2 in the reactor effluent stream (Fig. 2). Only at low temperatures there exist some slight deviations between the predicted and the measured concentrations of CO_2. At a temperature of 125 °C, it is clear that the model recognizes two separate peaks. The CO_2 response reaches its first maximum in the first few seconds. The second peak is not perfectly visible, but still, it is recognizable in a wide shoulder that is formed after the first peak as shown in the inset of Fig. 2b. If the temperature is increased to 150 °C, the second peak can be clearly identified. This is even more pronounced at a temperature of 200 °C, while at 250 °C, a very distinct transition from the first to second peak is evident. Even more, the model accurately predicts the shift of the maximum of second peak in the temperature range between 125 and 250 °C.

From the inset of Fig. 2b it is clear that the model predictions at 125 and 150 °C have a very different shape compared to the predictions at 75 and 100 °C, where only one maximum exists. At these temperatures, the maxima of first and second peak run one into another so that the model is not able to differentiate between the two. Indeed, if we examine carefully the circles in the inset of Fig. 2b representing experimental measurements at a reaction temperature of 100 °C, the circle at time equal to 3 s could represent the maximum of a first peak. However, only one data point is not enough for the model to distinguish between the two maxima. At a temperature of 75 °C, the discrimination between the two maxima could not be made anymore. Instead of two peaks, the model predicts only one peak at temperatures between 50 and 100 °C. This leads to a wrong estimation of kinetic constants at lower temperatures.

As discussed previously, the reaction steps 1 and 2 from Table 2 govern very fast responses of the CO_2 peak in CO oxidation over nanostructured $Cu_{0.1}Ce_{0.9}O_{2-y}$ catalysts. On the other hand, the height of a second peak is governed by reaction steps 3 to 6 that represent reoxidation of a reduced surface by subsurface lattice oxygen. If those two separate processes are slow, the two peaks in the CO_2 signal cannot be distinguished. This happens at lower temperatures. At higher temperatures, two distinct peaks are visible. This transition happens at 125 °C which is clearly represented in the inset of Fig. 2b. If we recall the CO-TPR experiments of nanostructured $Cu_{0.1}Ce_{0.9}O_{2-y}$ catalyst (Fig. 1) it can be seen that 125 °C is exactly the temperature where the onset

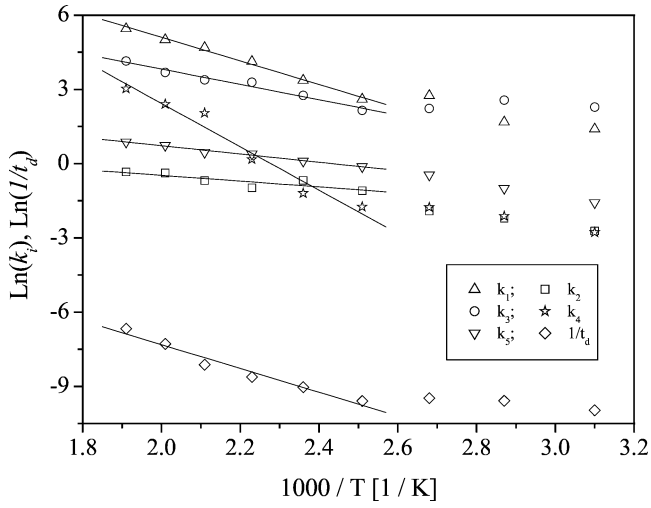

Fig. 6. Arrhenius plots of the kinetic parameters for the CO concentration step-change experiments. The results obtained at six different temperatures (from 125 to 250 °C with 25 °C increments) were included in the calculation of parameters given in Table 5.

Table 5
Estimates of the kinetic parameters obtained by regression of He → 1 vol% CO/He concentration step experiments for the CO oxidation over fully oxidized catalyst without the presence of oxygen in the reactor feed gas

$\ln A_1$ ($m^3\,mol^{-1}\,s^{-1}$)	14.6 ± 1.2
E_1 (kJ mol^{-1})	39.6 ± 4.6
$\ln A_2$ (s^{-1})	1.85 ± 2.1
E_2 (kJ mol^{-1})	9.7 ± 8.1
$\ln A_3$ ($m^3\,mol^{-1}\,s^{-1}$)	10.0 ± 1.6
E_3 (kJ mol^{-1})	25.8 ± 5.9
$\ln A_4$ ($kg_{cat}\,mol^{-1}\,s^{-1}$)	19.9 ± 5.2
E_4 (kJ mol^{-1})	72.9 ± 19.8
$\ln A_5$ ($m^3\,mol^{-1}\,s^{-1}$)	4.07 ± 0.63
E_5 (kJ mol^{-1})	13.9 ± 2.3
$\ln A_{td}$ (s^{-1})	2.29 ± 2.74
E_{td} (kJ mol^{-1})	40.0 ± 10.3

The parameters are obtained in the temperature span between 125 and 250 °C. The mass balance equations are given in Table 3, while the corresponding initial and boundary conditions are given in Table 4. The catalyst capacities are equal to $L_{TOT} = 0.030$ mol kg_{cat}^{-1}, $H_{TOT} = 0.35$ mol kg_{cat}^{-1}, F_{TOT} values correspond to Table 1 subtracted by 0.030 mol kg_{cat}^{-1}.

of the consumption of subsurface lattice oxygen begins. The results found by He → CO/He step experiments and CO-TPR experiments are in a complete agreement.

Fig. 6 represents Arrhenius plots of the rate constants k_1 to k_5 and reverse characteristic diffusion time $1/t_d = D/R^2$ for the He → 1 vol% CO/He concentration step over the nanostructured $Cu_{0.1}Ce_{0.9}O_{2-y}$ catalyst with no oxygen present in the reactor feed. Six experimental points (at temperatures from 125 to 250 °C with 25 °C increments) were included in the calculation of activation energies and preexponential factors of particular rate constant. The corresponding values of activation energies and preexponential factors are listed in Table 5. Because the confidence intervals were added to values of each parameter, preexponential factors are written in logarithmic form. Since the model is not able

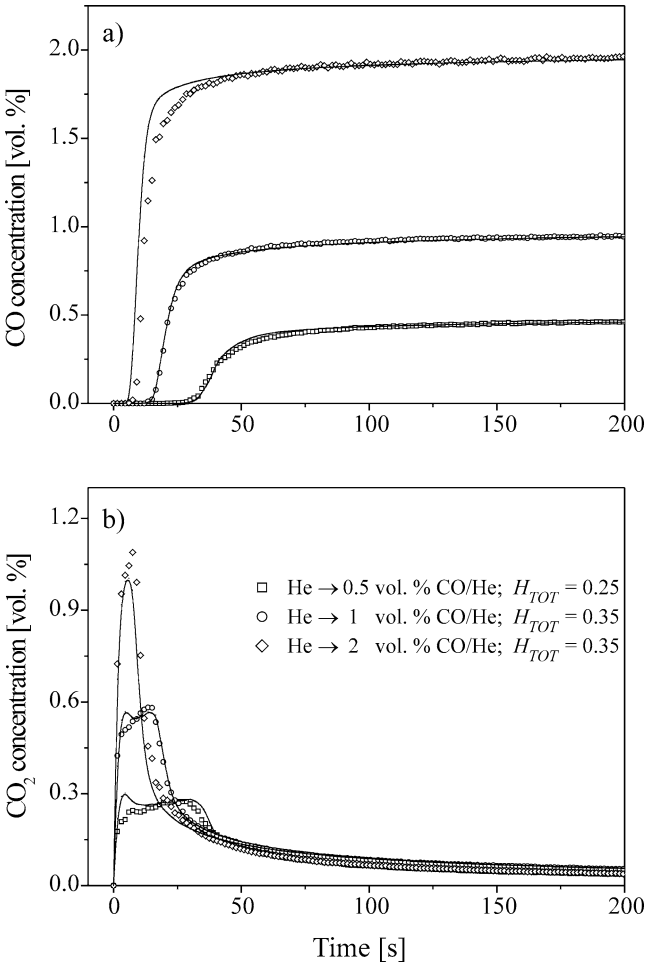

Fig. 7. (a) CO and (b) CO_2 concentrations in the reactor effluent stream as a function of CO concentration in reactor inlet steam at a temperature of 200 °C. The markers represent experiments and solid lines represent the model predictions. The rate equations are given in Table 3 with corresponding initial and boundary conditions given in Table 4. The kinetic parameter values are given in Table 5. $L_{\mathrm{TOT}} = 0.030\ \mathrm{mol\,kg_{cat}^{-1}}$, F_{TOT} values correspond to Table 1 subtracted by $0.030\ \mathrm{mol\,kg_{cat}^{-1}}$. Conditions: $m_{\mathrm{cat}} = 200$ mg, $\Phi_{\mathrm{v}} = 200\ \mathrm{mL\,min^{-1}}$.

to differentiate between first and second peaks at temperatures 50 to 100 °C, it does not predict accurately the kinetic constants. This is clearly visible from the shift in slopes of Arrhenius plots corresponding to all kinetic parameters at a temperature of 125 °C. Thus, the three experimental points corresponding to temperatures between 50 and 100 °C are excluded from the calculation of activation energies and preexponential factors.

Fig. 7 represents simulated responses of CO and CO_2 at a reaction temperature of 200 °C and at three different concentrations of CO in the reactor inlet stream. The model adequately predicts responses at all three concentrations of carbon monoxide. Kinetic parameters as obtained from the regression of model equations to the experimental responses with 1 vol% CO/He were used to calculate the responses with 0.5 and 2 vol% CO/He in the reactor inlet stream. However, one slight adaptation had to be performed before that. When concentration steps with 0.5 vol% CO/He were used, the OSC of a catalyst is 30% lower if compared to concentration steps with 1 vol% CO/He as explained in Section 3.3. Because of that, the volumetric capacity of catalyst, H_{TOT}, was set to $0.25\ \mathrm{mol\,kg_{cat}^{-1}}$ for the simulation of step experiments with 0.5 vol% CO in He.

In order to check the reliability of the model, the sensitivity of the proposed model on each parameter was evaluated. It was found that the model is most sensitive to changes in three catalyst capacities in the following order: it is most sensitive to changes in L_{TOT}, then to changes in H_{TOT}, and at last to changes in F_{TOT}. The sensitivity of the model to the change of diffusion coefficient is in the range of sensitivity to the change in F_{TOT}. The model is roughly an order of magnitude less sensitive to changes in five kinetic parameters.

The capacities of catalyst phases are usually hard to predict accurately. Therefore, we estimated the optimum values of kinetic parameters when changing the values of catalyst capacities for ±50% from the values that are given in Table 5. By varying the values of L_{TOT}, F_{TOT}, and H_{TOT} it was found that the activation energies of each parameter do not change at all. However, the variations in catalyst capacities had an effect on the preexponential factor of each parameter. This resulted only in the vertical shifts and not in the shifts in slope of Arrhenius plots in Fig. 6. It should be noted that the most drastic shifts were found if the capacity of catalyst active sites, L_{TOT}, was lowered to −50%. In this case, the optimum values of the preexponential factors of kinetic rate constants k_2, k_3, and k_4 were an order of magnitude higher than those reported in Table 5. This is not a surprise, because those reaction constants are directly connected with the surface reaction of CO on catalyst active sites. If we decrease the number of catalyst active sites, we must increase the values of kinetic rate constants in order to cope with the same experimentally measured rates.

The Arrhenius parameters corresponding to surface reaction steps 1, 2, 3, 6, and 7 of Table 2 are small if they are compared to the values expected for Langmuir–Hinshelwood type of surface reactions [49]. However, as already discussed, the CO oxidation over nanostructured $Cu_{0.1}Ce_{0.9}O_{2-y}$ catalyst does not proceed by this type of surface reaction. As shown by other authors, apparent activation energies between 14.2 and 50.1 kJ/mol are typical of various surface reactions over a nanostructured $Cu_{0.1}Ce_{0.9}O_{2-y}$ catalyst [43,50,51]. This is in agreement with apparent activation energies between 9.7 and 39.6 kJ/mol measured for surface reactions that were considered in this study. The weak temperature dependency of reaction rates is evident from the OSC measurements of that catalyst. Only around 5 times more CO_2 is formed at 250 °C compared with a quantity formed at 50 °C. These results are also in agreement with the results obtained for transient CO oxidation over a $Pt/Rh/CeO_2/y\text{-}Al_2O_3$ catalyst [7]. The adsorption of molecular CO was assumed to be a non-activated process in that study. The reaction rate

coefficient for CO adsorption on a site already covered by oxygen species was reported to be 4.61×10^3 m^3 mol^{-1} s^{-1}. In this work, the reaction rate coefficients k_1 and k_3 corresponding to reaction steps 1 and 3 have values of 2.33×10^2 and 0.64×10^2 m^3 mol^{-1} s^{-1}, respectively, at 250 °C and are weakly dependent on the reaction temperature. The results for the surface reaction of CO toward CO_2 on sites already covered by oxygen species, corresponding to reaction steps 2 and 6 in the model, are even more close. In [7], the preexponential factor and activation energy for that reaction were estimated to have values of 2.05×10^1 s^{-1} and 12.1 kJ mol^{-1}, respectively, while in the present work, preexponential factor and activation energy were estimated to have values of 0.64×10^1 s^{-1} and 9.7 kJ mol^{-1}. The molecular adsorption of CO on the catalyst inert sites, corresponding to reaction step 7, is also a weak function of temperature (see Fig. 6 and Table 5). This is in agreement with [52], where weak chemisorption of CO on metallic copper is reported.

The highest temperature dependency of CO oxidation over a nanostructured $Cu_{0.1}Ce_{0.9}O_{2-y}$ catalyst without the oxygen present in the reactor feed gas is found for the reaction step 5, representing reoxidation of reduced $COCu^+\square_s$ sites by subsurface lattice oxygen. Since the open literature on such reactions is very scarce, it is not possible to compare the data obtained in the present study to similar results. However, the activation energy for the catalyst reoxidation step (E_4 from Table 5) is close to 60.2×10^3 kJ mol^{-1} obtained in steady-state measurements for the selective CO oxidation in excess of H_2 over the nanostructured $Cu_{0.1}Ce_{0.9}O_{2-y}$ catalyst [4].

As already mentioned in Section 3.4, the copper active sites of a $Cu_{0.1}Ce_{0.9}O_{2-y}$-nanostructured catalyst are located on tiny needles. It was measured [44] that those needles have a radius equal to 500 nm. Now, from the definition of the characteristic diffusion time, it is possible to calculate the diffusion coefficient of oxygen species in the bulk $Cu_{0.1}Ce_{0.9}O_{2-y}$ crystallite lattice. At 250 °C, the diffusion coefficient equals to 3.2×10^{-12} cm^2 s^{-1}. The activation energy for the oxygen diffusion in nanostructured $Cu_{0.1}Ce_{0.9}O_{2-y}$ catalyst equals to 40.0 kJ mol^{-1} (Table 5). Those two values can be compared to the values obtained with similar catalysts.

The activation energy of oxygen diffusion in a $Ce_{0.69}Gd_{0.31}O_{2-y}$ catalyst measured at 600–1000 °C is reported to be 112 kJ mol^{-1}. The diffusion coefficient at a temperature of 250 °C as extrapolated by authors is equal to 1×10^{-12} cm^2 s^{-1} [40]. In a similar study, the activation energy of oxygen diffusion in $Zr_{0.81}Y_{0.19}O_{2-y}$ and in $Ce_{0.9}Gd_{0.1}O_{2-y}$ catalysts measured at 500–1100 °C is reported to be 96 and 87 kJ mol^{-1} [53], respectively, and the diffusion coefficient obtained by extrapolation of Arrhenius plot down to 250 °C is found to be equal to 9.5×10^{-14} and 2×10^{-12} cm^2 s^{-1}, respectively. Those two studies were performed by measuring oxygen self-diffusion by isotopic $^{18}O_2$ exchange over the surface. On the other hand, it was found that the diffusion of oxygen in the fluorite lattice of pure ceria is a function of the degree of reduction. In the very early stage of reduction, the number of vacancies is small and the activation energy is high. With further reduction, the number of vacancies in the fluorite structure grows i.e. more space for the diffusion of oxygen ions is available. As a consequence, the activation energy of oxygen diffusion is lowered [54,55]. For instance, the activation energies of oxygen diffusion in CeO_2, $CeO_{1.92}$, and $CeO_{1.80}$ measured at 800–1200 °C are reported to be 103, 50 and 15 kJ mol^{-1} [54], respectively. If we extrapolate the Arrhenius plots from that study down to 250 °C, we get that the diffusion coefficients of the three CeO_{2-y} species are equal to 1×10^{-13}, 2×10^{-10}, and 3×10^{-7} cm^2 s^{-1}, respectively. In the present study, the activation energies were measured by reduction of the nanostructured $Cu_{0.1}Ce_{0.9}O_{2-y}$ catalyst by carbon monoxide. Much greater reduction potential exists in the case of catalyst reduction by CO as compared to measurements of oxygen self-diffusion by isotopic exchange. A lower activation energy measured in the present study agrees with that facts.

It must be noted that extrapolations of Arrhenius plots as performed above can also be deceiving. It was shown that in the temperature range from 200 to 1000 °C the activation energy for the bulk conductivity of various $(1-x)ZrO_2/xCeO_2$ systems (x ranging from 0.5 to 1) is around 40% higher if measured at high temperatures as compared to measurements at low temperatures [56]. In the latter study, bulk conductivity is reported to have an electronic and ionic contribution. Since the ionic transference number was not measured under 500 °C and also ionic conductivity was not measured directly it cannot be said with great certainty what is the reason for the drop of activation energy in the low-temperature region. Nevertheless, this change in activation energy with temperature could also be a reason for different measurements of activation energy in the above studies and in the present study.

By using the diffusion coefficient as obtained in the present study, it is possible to estimate the average displacement of O^{2-} ion in the nanostructured $Cu_{0.1}Ce_{0.9}O_{2-y}$ catalyst by using the Einstein relation [57]:

$$\langle \bar{x} \rangle = (Dt)^{1/2}. \tag{3}$$

For a diffusion time equal to 30 s, the O^{2-} ion in the catalyst lattice travels a distance equal to 98 nm at a temperature of 250 °C.

Now, let us estimate the molar flow of oxygen ion species from the bulk of the catalyst to the catalyst surface of a nanostructured $Cu_{0.1}Ce_{0.9}O_{2-y}$ catalyst at the beginning of the CO concentration step. By using Fick's first law of diffusion, molar flux can be calculated [58] with the assumption of linear concentration gradient in the crystallite particle:

$$J_{O^{2-}} = D\frac{(C_b - C_s)}{R}. \tag{4}$$

In this approximation, the crystal structure of nanostructured $Cu_{0.1}Ce_{0.9}O_{2-y}$ catalyst was taken to be the fluorite

lattice. The concentration of oxygen ions in fully oxidized catalyst then equals to 8.4×10^4 mol m^{-3}. If complete reduction of catalyst surface is assumed, the concentration of oxygen ions on the catalyst surface equals to 7.6×10^4 mol m^{-3}. By using the particle radius equal to 500 nm [44], molar flux of the O^{2-} ions from the bulk to the catalyst surface equals to 5.1×10^{-6} mol m^{-2} s^{-1}. Multiplying this result with the BET surface area and the mass of the catalyst, the molar flow of oxygen ion species from the catalyst bulk to the catalyst surface is estimated to be 2.3×10^{-5} mol s^{-1}. Let us compare this value with the molar flow of CO over the catalyst surface. By using the ideal gas law, the molar flow of carbon monoxide at 250 °C is estimated to be equal to 4.6×10^{-5} mol s^{-1}. The two values are completely comparable. This means that enough oxygen is transported through the catalyst lattice to oxidize almost all carbon monoxide passing over the catalyst surface. The above estimation and the estimation of the average displacement of the oxygen ion species in the catalyst lattice prove that the significant tailing of CO_2 response as "seen" by the mass spectrometer is caused by bulk oxygen ion diffusion in the catalyst crystallite lattice. Even more, the diffusion coefficient calculated by the model given in Table 3 has a correct value.

5. Conclusions and outlook

In the present study we have presented:

- How the reducibility of the nanostructured $Cu_{0.1}Ce_{0.9}O_{2-y}$ catalyst measured by CO temperature-programmed reduction experiments changes.
- How the oxygen-storage capacity of the nanostructured $Cu_{0.1}Ce_{0.9}O_{2-y}$ catalyst varies with reaction temperatures between 50 and 250 °C, as determined by CO concentration step experiments.
- A detailed kinetic model based on elementary reaction steps for CO oxidation over a nanostructured $Cu_{0.1}Ce_{0.9}O_{2-y}$ catalyst. The model is capable of accurately predicting the concentrations of CO and CO_2 in the reactor effluent stream if it operates under dynamic conditions.
- The bulk oxygen diffusion coefficient equal to 3.2×10^{-12} cm^2 s^{-1} at 250 °C as calculated by the model.
- That the nanostructured $Cu_{0.1}Ce_{0.9}O_{2-y}$ catalyst has a great potential as a future PROX reactor catalyst, because of the large oxygen-storage capacity and high selectivity toward CO oxidation.

It should be noted that the redox mechanism that was used to model dynamic behavior of CO oxidation is consistent with our previous study, where we modeled selective CO oxidation under a steady-state mode of operation [4].

Further studies employing concentration cycling of CO/$^{16}O_2$ [59] as well as CO/$^{18}O_2$ in the reactor inlet stream are in progress. These studies will reveal also the kinetics of catalyst reoxidation step by gas-phase oxygen. Apart from that, the CO/$^{18}O_2$ concentration cycling responses will be confronted by the transient kinetic model predictions of species that are located on the catalyst surface and are denoted by $Cu^{2+}O_{s,s}$, $CO\cdots Cu^{2+}O_{s,s}$, $Cu^{+}\square_s$, $CO\cdots Cu^{+}\square_s$, and $CO\cdots Cu^{2+}O_{s,b}$ in the present study. It will be shown that the transient kinetic model as developed in the present study predicts accurately also kinetics occurring on the catalyst surface.

6. Nomenclature

a	Specific surface area of a catalyst particle, $m^2_{\text{external surface}}\, m^{-3}_{\text{particle}}$
A_i	Preexponential factor of the rate constant i, various units
A_{td}	Preexponential factor of the reverse oxygen diffusion coefficient, cm^2 s^{-1}
C_{b}	Concentration of O^{2-} ions in bulk catalyst, mol m^{-3}
C_{S}	Concentration of O^{2-} ions on the surface of the catalyst, mol m^{-3}
C_{TOT}	Total molar concentration of gas phase, $\text{mol}\, m^{-3}_{\text{gas}}$
D	Diffusion coefficient of oxygen species in the solid catalyst lattice, m^2 s^{-1}
E_i	Activation energy of the rate constant i, kJ mol^{-1}
E_{td}	Activation energy of the reverse oxygen diffusion coefficient, kJ mol^{-1}
F_{TOT}	Surface capacity of catalyst inert phase, $\text{mol}\, kg^{-1}_{\text{cat}}$
H_{TOT}	Volumetric capacity of catalyst, $\text{mol}\, kg^{-1}_{\text{cat}}$
$J_{O^{2-}}$	Molar flux of O^{2-} ions from the bulk to the catalyst surface, mol m^{-2} s^{-1}
k_1	Rate constant of elementary reaction step 1, m^3 mol^{-1} s^{-1}
k_2	Rate constant of elementary reaction steps 2 and 6, s^{-1}
k_3	Rate constant of elementary reaction step 3, m^3 mol^{-1} s^{-1}
k_4	Rate constant of elementary reaction step 5, kg_{cat} mol^{-1} s^{-1}
k_5	Rate constant of elementary reaction step 7, m^3 mol^{-1} s^{-1}
L_{TOT}	Surface capacity of catalyst active phase, $\text{mol}\, kg^{-1}_{\text{cat}}$
m_{cat}	Mass of catalyst, kg
R	Crystallite radius, m
t	Time, s
t_{d}	Characteristic diffusion time, s
x	Dimensionless radial position in catalyst crystallite particle
$\langle\bar{x}\rangle$	Average displacement of O^{2-} species in the bulk catalyst lattice, m
y_i	Molar fraction of gas component i
z	Dimensionless distance of catalyst bed

6.1. Greek letters

δ_n	Fractional surface coverage of species n adsorbed on catalyst inert phase
ε_B	Void fraction of catalyst bed = 0.35
Φ_v	Total volumetric flow rate at reaction conditions, $m^3_{gas}\ s^{-1}$
ρ_B	Catalyst bulk density, $kg_{cat}\ m_r^{-3}$
θ_j	Fractional surface coverage of species j adsorbed on catalyst active phase
τ	Space time, s
ξ_m	Fractional volumetric "coverage" of species m that diffuses through the catalyst particle

6.2. Subscripts

b	Oxygen vacancy located in the catalyst bulk lattice
s	Oxygen vacancy located on the catalyst surface
b, b	Oxygen species located in the catalyst bulk lattice, that originated in the bulk
s, b	Oxygen species located on the catalyst surface, that originated from the bulk catalyst lattice
s, s	Oxygen species located on the catalyst surface, that originated on the catalyst surface

Acknowledgment

The authors gratefully acknowledge the financial support of the Ministry of Education, Science, and Sport of the Republic of Slovenia through the Grant P0-0521-0104.

References

[1] S. Hočevar, J. Batista, H. Matralis, T. Ioannides, G. Avgouropoulos, PCT Application No. PCT/SI01/00005, 2001.
[2] G. Avgouropoulos, T. Ioannides, H.K. Matralis, J. Batista, S. Hočevar, Catal. Lett. 73 (2001) 33.
[3] G. Avgouropoulos, T. Ioannides, Ch. Papadopoulou, J. Batista, S. Hočevar, H.K. Matralis, Catal. Today 75 (2002) 157.
[4] G. Sedmak, S. Hočevar, J. Levec, J. Catal. 213 (2003) 135.
[5] G. Avgouropoulos, T. Ioannides, Appl. Catal. A 244 (2003) 155.
[6] M. Flytzani-Stephanopoulos, MRS Bull. November (2001) 885.
[7] R.H. Nibbelke, A.J.L. Nievergeld, J.H.B.J. Hoebink, G.B. Marin, Appl. Catal. B 19 (1998) 245.
[8] A. Renken, Int. Chem. Eng. 33 (1) (1993) 61.
[9] K. Tamaru, Appl. Catal. A 151 (1997) 167.
[10] H. Kobayashi, M. Kobayashi, Catal. Rev.-Sci. Eng. 10 (2) (1974) 139.
[11] C.O. Bennett, Adv. Catal. 44 (2000) 329.
[12] P. Silveston, R.R. Hudgins, A. Renken, Catal. Today 25 (1995) 91.
[13] P.L. Silveston, Can. J. Chem. Eng. 69 (October) (1991) 1106.
[14] E. Gulari, X. Zhou, C. Sze, Catal. Today 25 (1995) 145.
[15] F.H.M. Dekker, G. Klopper, A. Bliek, F. Kapteijn, J.A. Moulijn, Chem. Eng. Sci. 49 (1994) 4375.
[16] F.J.R. van Neer, B. van der Linden, A. Bliek, Catal. Today 38 (1997) 115.
[17] H. Randall, R. Doepper, A. Renken, Ind. Eng. Chem. Res. 36 (1997) 2996.
[18] S. Hočevar, U. Opara Krašovec, B. Orel, A.S. Arico, H. Kim, Appl. Catal. B 28 (2000) 113.
[19] A.M. Efstathiou, X.E. Verykios, Appl. Catal. A 151 (1997) 109.
[20] O. Levenspiel, Chemical Reaction Engineering, Wiley, New York, 1972.
[21] P. Zimmer, A. Tschöpe, R. Birringer, J. Catal. 205 (2002) 339.
[22] W. Liu, M. Flytzani-Stephanopoulos, Chem. Eng. J. 64 (1996) 283.
[23] J. Xiaoyuan, L. Guanglie, Z. Renxian, M. Jianxin, C. Yu, Z. Xiaoming, Appl. Surf. Sci. 173 (2001) 208.
[24] J.B. Wang, S.-C. Lin, T.-J. Huang, Appl. Catal. A 232 (2002) 107.
[25] A. Badri, J. Lamotte, J.C. Lavalley, A. Laachir, V. Perrichon, O. Touret, G.N. Sauvion, E. Quemere, Eur. J. Solid State Inorg. Chem. 28 (1991) 445.
[26] G. Sedmak, PhD thesis, University of Ljubljana, Ljubljana, Slovenia, 2003.
[27] M. Kobayashi, Chem. Eng. Sci. 37 (3) (1982) 393.
[28] T.X.T. Sayle, S.C. Parker, C.R.A. Catlow, Surf. Sci. 316 (1994) 329.
[29] A.Q.M. Boon, F. van Looij, J.W. Geus, J. Mol. Catal. 75 (1992) 277.
[30] C. Li, Y. Sakata, T. Arai, K. Domen, K.-I. Maruya, T. Onishi, J. Chem. Soc., Faraday Trans. 85 (1989) 929.
[31] A. Martinez-Arias, M. Fernandez-Garcia, O. Galvez, J.M. Coronado, J.A. Anderson, J.C. Conesa, J. Soria, G. Munuera, J. Catal. 195 (2000) 207.
[32] C.Y. Ying, A. Tschöpe, Chem. Eng. J. 64 (1996) 225.
[33] J. Xiaoyuan, Z. Renxian, Y. Jun, L. Guanglie, Z. Xiaoming, J. Rare Earths 22 (2003) 55.
[34] J.J. Zhang, Y.J. Liu, N. Li, B.X. Lin, Acta Phys.-Chim. Sin. 15 (1999) 15.
[35] P. Bera, K.R. Priolkar, P.R. Sarode, M.S. Hegde, S. Emura, R. Kumashiro, N.P. Lalla, Chem. Mater. 14 (2002) 3591.
[36] S. Hočevar, J. Batista, J. Levec, J. Catal. 184 (1999) 39.
[37] C. Lamonier, A. Ponchel, A. D'Huysser, L. Jalowiecki-Duhamel, Catal. Today 50 (1999) 247.
[38] P. Bera, S. Mitra, S. Sampath, M.H. Hedge, Chem. Commun. (2001) 927.
[39] A. Tschöpe, J.Y. Ying, H.L. Tuller, Sens. Actuators B 31 (1996) 111.
[40] E. Ruiz-Trejo, J.D. Sirman, Y.M. Baikov, J.A. Kilner, Solid State Ionics 113–115 (1998) 565.
[41] A. Marines-Arias, M. Fernandez-Garcia, J. Soria, J.C. Conesa, J. Catal. 182 (1999) 367.
[42] P.G. Harrison, I.K. Ball, W. Azelee, W. Daniell, D. Goldfarb, Chem. Mater. 12 (2000) 3715.
[43] W. Liu, M. Flytzany-Stephanopoulos, J. Catal. 153 (1995) 317.
[44] S. Hočevar, J. Levec, Abstr. Pap. Am. Chem. S. 222: 249-COLL, Part 1 (2001).
[45] J. Crank, The Mathematics of Diffusion, Clarendon, Oxford, 1986.
[46] G.D. Smith, Numerical Solution of Partial Differential Equations. Finite Difference Methods, Clarendon, Oxford, 1996.
[47] R. Macey, G. Oster, T. Zahnley, Berkeley Madonna User's Guide, Univ. of California, 1999.
[48] A. Dandekar, M.A. Vannice, J. Catal. 178 (1998) 621.
[49] V.P. Zhdanov, Surf. Sci. Rep. 12 (1991) 183.
[50] M. Kobayashi, M. Flytzani-Stephanopoulos, Ind. Eng. Chem. Res. 41 (2002) 3115.
[51] Y. Li, Q. Fu, M. Flytzani-Stephanopoulos, Appl. Catal. B 27 (2000) 179.
[52] D.A. King, D.P. Woodruff, Chemisorption Systems. Part A, in: The Chemical Physics of Solid Surfaces and Heterogeneous Catalysis, vol. 3, Elsevier, Amsterdam, 1990.
[53] P.S. Manning, J.D. Sirman, J.A. Kilner, Solid State Ionics 93 (1997) 125.
[54] J.M. Floyd, Ind. J. Technol. 11 (11) (1973) 589.
[55] H. Inaba, H. Tagawa, Solid State Ionics 83 (1996) 1.
[56] C. Chiodelli, G. Flor, M. Scagliotti, Solid State Ionics 91 (1996) 109.
[57] A. Trovarelli, M. Boaro, E. Rocchini, C. de Leitenburg, G. Dolcetti, J. Alloys Comp. 323–324 (2001) 584.
[58] M. Boaro, C. de Leitenburg, G. Dolcetti, A. Trovarelli, J. Catal. 193 (2000) 338.
[59] G. Sedmak, S. Hočevar, J. Levec, in press.